The Journal of Chemical Physics

Fifth-order two-quantum absorptive two-dimensional electronic spectroscopy of CdSe quantum dots

Cite as: J. Chem. Phys. **153**, 234703 (2020); https://doi.org/10.1063/5.0021381
Submitted: 10 July 2020 . Accepted: 26 November 2020 . Published Online: 15 December 2020

Patrick Brosseau, Samuel Palato, Hélène Seiler, Harry Baker, and Patanjali Kambhampati

The Journal of Chemical Physics ARTICLE scitation.org/journal/jcp

Fifth-order two-quantum absorptive two-dimensional electronic spectroscopy of CdSe quantum dots

Cite as: J. Chem. Phys. 153, 234703 (2020); doi: 10.1063/5.0021381
Submitted: 10 July 2020 • Accepted: 26 November 2020 •
Published Online: 15 December 2020

Patrick Brosseau, Samuel Palato,[a] Hélène Seiler,[a] Harry Baker, and Patanjali Kambhampati[b]

AFFILIATIONS

Department of Chemistry, McGill University, Montreal, Quebec H3A 0B8, Canada

[a]**Present address:** Department of Physical Chemistry, Fritz Haber Institute of the Max Planck Society, Faradayweg 4-6, 14195 Berlin, Germany.
[b]**Author to whom correspondence should be addressed:** pat.kambhampati@mcgill.ca

ABSTRACT

Two-quantum variants of two-dimensional electronic spectroscopy (2DES) have previously been used to characterize multi-exciton interactions in molecules and semiconductor nanostructures though many implementations are limited by phasing procedures or non-resonant signals. We implement 2DES using phase-cycling to simultaneously measure one-quantum and two-quantum spectra in colloidal CdSe quantum dots. In the pump–probe geometry, fully absorptive spectra are automatically acquired by measuring the sum of the rephasing and nonrephasing signals. Fifth-order two-quantum spectroscopy allows for direct access to multi-exciton states that may be obscured in excited state absorption signals due to population relaxation or third-order two-quantum spectra due to the non-resonant response.

I. INTRODUCTION

Optical excitation of semiconductor quantum dots (QDs) forms bound electron–hole pairs, or excitons (X). QDs may simultaneously confine several excitons, which form confined multi-excitons (MX). The energy of an MX state is characterized by a binding energy, Δ_{MX}, which reflects mean-field effects as well as correlation interactions.[1] The MX state is split into a fine structure, and this fine structure varies depending on the size of the QD.[2,3] Characterization of the MX fine structure in semiconductor nanostructures is therefore important for understanding material properties such as optical gain[4] as well as testing fundamental many-body physics.

Coherent multi-dimensional spectroscopy (CMDS) reveals electronic and vibrational structure dynamics on an ultrafast timescale by correlating the time evolution of quantum coherences. CMDS typically employs one-quantum (1Q) coherences, giving insight into phenomena such as spectral diffusion[5] and electronic and vibrational couplings.[6,7] Two-quantum (2Q) coherences are a promising probe for many-body physics as they directly excite two-photon transitions, reflecting electron correlation effects[8–12] and multi-exciton dynamics.[13] However, third-order 2Q CMDS is restricted to non-rephasing pathways and may be contaminated with the non-resonant response due to the lack of a time delay between the pump and probe pulses.[14]

Fifth-order CMDS offers a greater number of excitation pathways than third-order CMDS, allowing one to disentangle signals that are obscured in lower-order implementations.[6,15–19] Fifth-order 2Q CMDS has been used to isolate MX signals in semiconductor nanostructures,[11,20] distinguishing bound biexcitons and unbound two-exciton correlations.[20] Recently, fifth-order 2Q CMDS has been used to study exciton–exciton interactions in molecular aggregates.[13,21–24] Fifth-order 2Q CMDS allows for measurement of both rephasing and non-rephasing 2Q signals[25] and allows for a time delay between pump and probe pulses, which may help to avoid the non-resonant response seen in third-order 2Q spectra.

Many 2Q spectra have been measured in the BOXCARS beam geometry, where desired signals are isolated using phase-matching.[8,10–12,20,26] One often desires to combine rephasing and non-rephasing signals to generate "fully absorptive" spectra. Due

to the inherent phase instability of non-collinear beam geometries, individual signals must be phase-shifted before combination and typical phasing procedures may not be reliable for the 2Q signal.[26] Phase instability in the BOXCARS beam geometry can be circumvented with active or passive phase stabilization procedures, which contribute to experimental complexity.[10,27,28] Conversely, collinear beam geometries isolate the desired signal by cycling the phase of the excitation pulses.[29–31] Fluorescence-detected collinear beam geometries allow for isolation of multiple 2Q signals,[32,33] and the partially collinear pump–probe geometry allows for isolation of a fully absorptive fifth-order 2Q signal.[13,24,25]

Here, we implement a two-dimensional electronic spectroscopy (2DES) experiment in the pump–probe geometry, employing four-step phase-cycling to simultaneously and separately measure fully absorptive 1Q and 2Q spectra in colloidal CdSe QDs.

II. EXPERIMENTAL METHODS

The 2DES experiments presented here use three independently controlled pulses to prepare a macroscopic polarization. The pulses interact with the sample creating coherences, such as $|G\rangle\langle X|$, or exciton populations, such as $|X\rangle\langle X|$. A pump–probe beam geometry is used: the first two pulses are collinear and cross through the sample at an angle in the direction $k_1 = k_2$, while the third pulse passes straight through the sample in the direction k_3. The first and second pulses are separated by time delay t_1. The second and third pulses are separated by time delay t_2. The prepared polarization radiates during time delay t_3. The radiated signal is detected by a spectrometer as a function of t_1 and t_2, and oscillations along t_3 are directly detected in the frequency domain. In the pump–probe geometry, many signals are simultaneously detected in the k_3 direction; therefore, desired signals are isolated by phase-cycling. The phase difference between the first two pulses, $\Delta\phi_{12}$, is varied, and the signal is measured for every phase value. Linear combinations of the signal at different values of $\Delta\phi_{12}$ allow for the retrieval of the 1Q and 2Q spectra. Increasing the intensity of the first two pulses allows one to see multi-exciton signals that are not created at low intensities.

Multiple 1Q and 2Q signals are created in the three-pulse 2DES experiment. We will begin by comparing four signals that we label third-order 1Q, fifth-order 1Q, third-order 2Q, and fifth-order 2Q. The third-order and fifth-order signals are created by three and five pulse interactions, respectively. The first two pulses are high intensity pump pulses, allowing for several interactions per pulse, while the third pulse is a low intensity probe pulse. The third-order 2Q signal is created in this experiment but cannot be measured in the pump–probe geometry. This signal is presented purely for reference.

The four signals are depicted in Fig. 1 as schematic pulse diagrams and as wave-mixing energy level (WMEL) diagrams, on the left and right, respectively. A three level system with a ground state

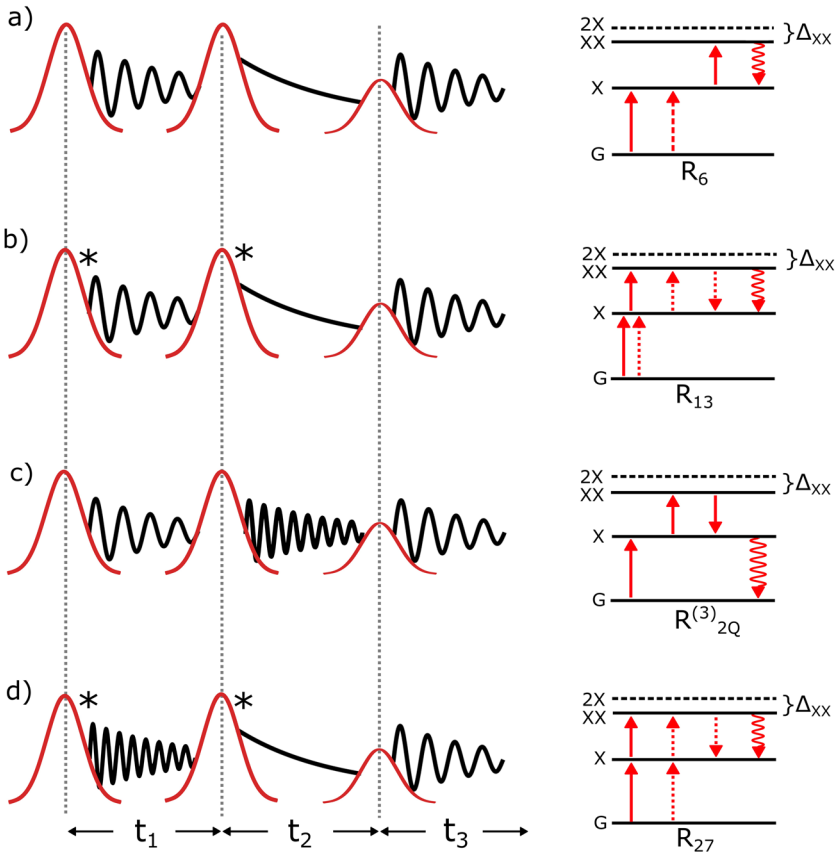

FIG. 1. Schematic representations of (a) third-order 1Q pathway $k_1 - k_2 + k_3$, (b) fifth-order 1Q pathway $(k_1 - k_1) + k_1 - k_2 + k_3$, (c) third-order 2Q pathway $k_1 + k_2 - k_3$, and (d) fifth-order 2Q pathway $2k_1 - 2k_2 + k_3$. Asterisks denote that multiple interactions are possible with that pulse. On the right, the four pathways are depicted as level diagrams for a three level system with a binding energy Δ_{XX}. Solid arrows represent interaction with the *ket*, dashed arrows represent interaction with the *bra*, and a wavy arrow represents the emitted signal.

(G), a single exciton state (X), and a biexciton state (XX) is assumed. In a WMEL diagram, time moves forward from left to right, and each arrow corresponds to a single pulse interaction. A solid arrow corresponds to interaction with the *ket*, and a dashed arrow corresponds to interaction with the *bra*. A wavy arrow represents the emitted signal. The biexciton state is shifted to a lower energy than twice the single exciton energy (2X). This shift, Δ_{XX}, corresponds to the biexciton binding energy.

In the third-order 1Q experiment [Fig. 1(a)], the first pulse interacts with the system and creates a coherent superposition of the ground and singly excited states, or 1Q coherence. This macroscopic polarization oscillates during time delay t_1. After time delay t_1, the second pulse transfers the system from a coherence to a population that evolves during t_2. The third pulse creates a third-order polarization that oscillates during t_3 and radiates in the $k_1 - k_2 + k_3$ and $-k_1 + k_2 + k_3$ wavevector directions. In the pump–probe geometry, $k_1 = k_2$, so the signal simply radiates in the k_3 direction. The sum of the $k_1 - k_2 + k_3$ and $-k_1 + k_2 + k_3$ signals gives a fully absorptive spectrum, as typically measured in 2D spectroscopies.[34–37] An example pathway is shown in the WMEL diagram in Fig. 1(a).

The fifth-order 1Q pathways are created when an intense pump pulse interacts with the system several times, as depicted in Fig. 1(b). One example is the pathway $(k_1 - k_1) + k_1 - k_2 + k_3$ that radiates in the same direction as the third-order 1Q pathway $k_1 - k_2 + k_3$ and is shown in the WMEL diagram in Fig. 1(b). In this pathway, the first pulse interacts with the system three times, while the second and third pulses interact once each. These fifth-order 1Q signals can complicate the interpretation of 1Q spectra[37–39] and cannot be readily isolated from their third-order 1Q counterparts using phase-cycling, though these contributions can be distinguished based on their pulse intensity dependence.

In the third-order 2Q experiment [Fig. 1(c)], the first pulse creates a 1Q coherence and the second pulse creates a coherent superposition of the ground and doubly excited states, or 2Q coherence, which oscillates during time t_2. The third pulse creates a third-order polarization that oscillates during t_3 and radiates in the $k_1 + k_2 - k_3$ wavevector direction.[8–12] An example pathway is shown in Fig. 1(c). There is no rephasing equivalent to this pathway; therefore, a fully absorptive third-order 2Q spectrum cannot be generated. This leaves the spectrum with a phase twist, which can obscure the interpretation of the spectrum.[40] Additionally, this pathway does not allow for a population time delay between the two pump pulses and the final probe pulse. The overlap between these pulses can lead to unwanted non-resonant signals.[14] Because of phase-matching restrictions, the third-order 2Q signal cannot be measured in the pump–probe geometry.

In the fifth-order 2Q experiment, Fig. 1(d), the first pulse interacts with the system twice directly creating a 2Q coherence that oscillates during t_1. The second pulse then interacts twice creating a population, and the third pulse transfers the system to a 1Q coherence. The fifth-order polarization oscillates during t_3, radiating in the $-2k_1 + 2k_2 + k_3$ and $2k_1 - 2k_2 + k_3$ wavevector directions.[11,13,20] Summation of these two terms gives a fully absorptive fifth-order 2Q spectrum. In the pump–probe geometry, both these signals are detected in the k_3 direction.

The coherences along time t_3 are directly measured in the spectral domain in this experiment. Isolating the signal in the third-order 1Q and fifth-order 1Q signals and then Fourier transforming the coherence along time t_1 generate a 1Q–1Q spectral correlation map, or 1Q spectrum. Isolating the signal in the fifth-order 2Q signal and then Fourier transforming the coherence along time t_1 generate a 2Q–1Q spectral correlation map, or 2Q spectrum.

Cascaded third-order signals may be confused with fifth-order signals, and in some cases, the cascaded signals dominate the spectrum, as in fifth-order Raman spectroscopy.[41] Concentration studies have shown that third-order cascades do not contribute significantly to fifth-order order experiments that exclusively contain resonant transitions.[6,16,18] The cascaded signal depends on the sample concentration, sample thickness, excitation frequency, phase-matching geometry, and the relative intensity of the third-order and fifth-order response functions.[16] To minimize cascades, we have used an optical density of 0.3 mm and a 0.2 mm sample thickness, which would result in a cascade intensity that is similar to or smaller than other studies.[6,18] The optical frequency is also similar to previous studies.[6,18] To minimize the optical path length, the probe beam is aligned perpendicular to the face of the sample cell.

This paper presents a comparison of two 2DES signals extracted from the same experiment. The 1Q spectrum, including contributions from both third-order and fifth-order 1Q pathways, is compared to the 2Q spectrum, which is purely fifth-order. The 2DES measurements are performed on a previously described pulse-shaper based instrument.[36] A pump–probe beam geometry and a $4 \times 1 \times 1$ phase-cycling scheme are used, as discussed in Appendices B 1 and B 2. The phase of the first pulse is cycled through values of $\Delta\phi_{12} = 0$, $\pi/2$, π, and $3\pi/2$. The 1Q 2D spectrum is obtained using weights [1, 0, −1, 0]. The 2Q 2D spectrum is obtained using weights [1, −1, 1, −1]. The acquisition uses a rotating frame with a frequency of 307.45 THz to avoid aliasing in the 2Q coherence. The delay time t_1 is incremented in steps of 1 fs from 0 fs to 100 fs. The pump pulse energy was varied from 2.9 nJ/pulse to 35 nJ/pulse. While high pulse intensities are required to maximize fifth-order signals, artifacts in the pulse shape are possible when operating acousto-optic pulse shapers at high intensity. The highest intensity pulse used in this study was characterized using transient-grating frequency resolved optical gating (TG-FROG), as shown in Appendix A 2. The pulse duration is determined to be 12 fs, and no pulse shaper artifacts are evident. The 1Q and 2Q signals are apodized using Gaussian apodization windows with widths of $\sigma =$ 45 fs and 22.5 fs, respectively; details of the apodization are shown in Appendix A 3. The pump pulse powers were varied with the pulse shapers; then, the powers were independently measured with a power meter placed directly before the sample position. Colloidal CdSe QDs are provided by NNlabs and have absorption and emission linewidth characteristic of an ensemble dispersity of $\sigma < 10\%$. The sample is diluted to an optical density of 0.3 nm at 640 nm and flowed through a 0.2 mm flow cell. The sample absorption spectrum and laser spectrum are provided in Appendix A 1.

III. THEORY

In this section, we will list the pathways that are theoretically detected in the third-order 1Q, fifth-order 1Q, and fifth-order 2Q cases. For simplicity, we will limit our analysis to a three level system, corresponding to the doubly degenerate[3] band-edge state of a CdSe QD.

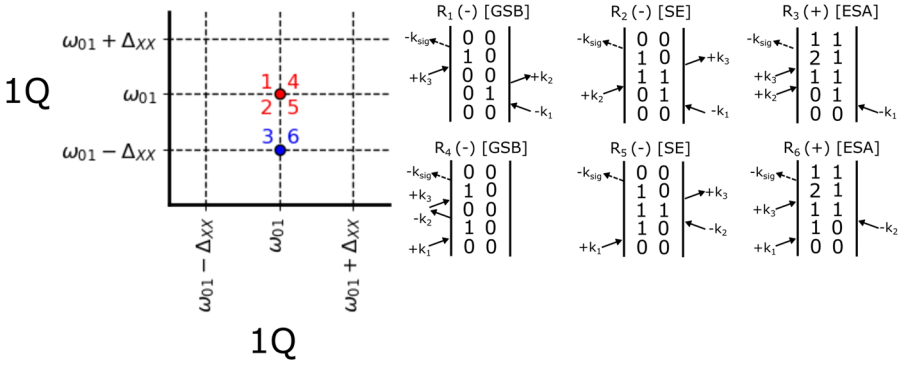

FIG. 2. Third-order contributions to the 1Q spectrum. Left: Peak positions for third-order 1Q. Positive signals are shown in blue, and negative signals are shown in red. Numbers correspond to numbered DSFDs. Right: (top row) rephasing pathways: $-k_1 + k_2 + k_3$, (bottom row) non-rephasing pathways: $k_1 - k_2 + k_3$. The sign of the signal is in parentheses.

The polarization $P(t)$ emitted after interaction with an electric field $E(t)$ is traditionally expressed perturbatively,[16,40] as in Eq. (1). Centrosymmetric systems do not emit even-order terms in the polarization as these orders rely on non-inversion symmetry,

$$P(t) = P^{(1)}(t) + P^{(3)}(t) + P^{(5)}(t) + \cdots \propto iR^{(1)}(t)E(t) + i^3R^{(3)}(t)E^3(t) + i^5R^{(5)}(t)E^5(t) + \cdots. \quad (1)$$

Here, $P^{(1)}$ is the first-order polarization as measured by a linear absorption experiment, $P^{(3)}$ is the third-order polarization as measured by the third-order 2DES experiment, and $P^{(5)}$ is the fifth-order polarization as measured by a fifth-order 2DES experiment. The terms $R^{(K)}(t)$ correspond to the Kth order response functions. Each term $R^{(K)}(t)$ is itself a sum of response functions, $R^{(K)}(t) = \sum_i R_i^{(K)}(t)$, where each $R_i^{(K)}$ corresponds to a distinct sequence of pulse interactions. In the following discussion, the label (K) is omitted, and the response functions are designated solely by the label i. In order to isolate a desired signal, these response functions may be discriminated by the direction of the emitted radiation and phase-cycling. This is discussed in detail in Appendices B 1 and B 2.

Figures 2–4 depict the third-order 1Q, fifth-order 1Q, and fifth-order 2Q signals, respectively, using double-sided Feynman diagrams (DSFDs). In a DSFD, time progresses from the bottom of the diagram to the top; the left side of the diagram represents the *ket*,

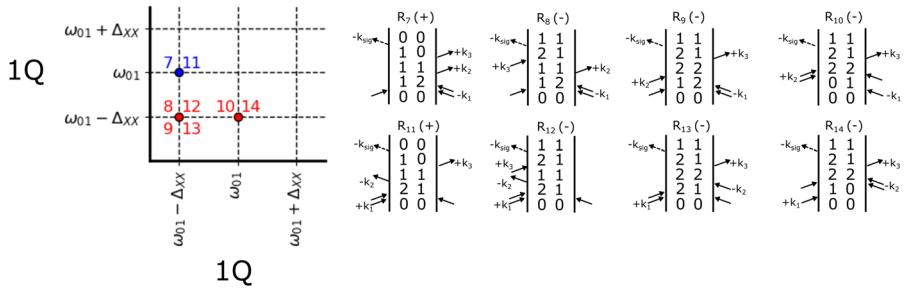

FIG. 3. Fifth-order contributions to the 1Q spectrum. (Left) Peak positions for fifth-order 1Q. Positive signals are shown in blue, and negative signals are shown in red. Numbers correspond to numbered DSFDs. (Right) DSFDs for fifth-order 1Q pathways. Other fifth-order 1Q pathways may be simplified and are identical to the third-order pathways in Fig. 2, so they are not included in this figure. Pathways including multiple interactions with the third pulse are omitted as the third pulse is of low intensity.

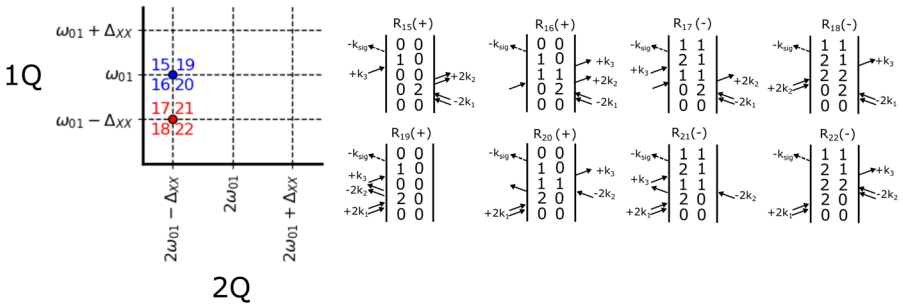

FIG. 4. Fifth-order 2Q pathways. Left: Peak positions for fifth-order 2Q signals. The x axis is at twice the frequency of the diagrams in Figs. 2 and 3. Positive signals are shown in blue, and negative signals are shown in red. Numbers correspond to numbered DSFDs. Right: (top row) rephasing pathways: $-2k_1 + 2k_2 + k_3$, (bottom row) non-rephasing pathways: $2k_1 - 2k_2 + k_3$.

and the right side represents the *bra*; arrows pointing toward the diagram represent excitation, while arrows pointing away represent emission; the final, dashed arrow represents the emitted signal. For readability, the ground state is denoted by 0, the X state is denoted by 1, and the XX state is denoted by 2.

For the third-order contributions to the 1Q experiment, six signals are detected: the wavevector sequence $-k_1 + k_2 + k_3$ results in the three rephasing pathways R_1, R_2, and R_3, and the sequence $k_1 - k_2 + k_3$ results in the three non-rephasing pathways R_4, R_5, and R_6. Diagrams R_1 and R_4 are ground-state bleach (GSB) signals, while R_2 and R_5 are stimulated emission (SE) and R_3 and R_6 are excited state absorption (ESA). The spectral positions of each DSFD are shown in a schematic in Fig. 2.

The fifth-order 1Q signals correspond to pathways $(-k_1 + k_1) - k_1 + k_2 + k_3$, $(-k_1 + k_1) + k_1 - k_2 + k_3$, $-k_1 + k_2 + (-k_2 + k_2) + k_3$, and $k_1 - k_2 + (-k_2 + k_2) + k_3$. In some cases, simultaneous pulse interactions acting on the same side of the DSFD but in opposite directions can negate each other. For this reason, fifth-order pathways may simplify and become identical to third-order pathways, although with a different sign due to the i^5 term in Eq. (1). These fifth-order signals would appear at the same position as the third-order pathways and decrease the intensity of the peak. For a three level system, there are eight cases of fifth-order pathways that do not simplify, and these DSFDs are shown in Fig. 3. Six of these cases are particularly significant as they feature $|1\rangle\langle 2|$ coherences along time delay t_1, which is not possible in any of the third-order 1Q pathways. This displaces the signal along excitation energy by the binding energy, Δ_{XX}.

In the case of the fifth-order 2Q experiment, eight pathways are detected for a three level system. The wavevector sequence $-2k_1 + 2k_2 + k_3$ results in the four rephasing pathways R_{15}, R_{16}, R_{17}, and R_{18}, and the sequence $2k_1 - 2k_2 + k_3$ results in the four non-rephasing pathways R_{19}, R_{20}, R_{21}, and R_{22}. As in the third-order 1Q case, diagrams R_{15} and R_{19} are GSB signals, R_{16} and R_{20} are SE, and R_{17} and R_{21} are ESA. In contrast to the third-order 1Q case, there are two XX SE diagrams, R_{18} and R_{22}. ESA to triexciton states from biexciton states is also possible but will have a limited effect in the bandwidth described here as the doubly degenerate band-edge electronic state in CdSe QDs does not allow for triexcitons.[3] This is further discussed in Fig. 7. Exciton–exciton annihilation as well as biexciton population relaxation[13] can cause a biexciton population $|2\rangle\langle 2|$ to relax to an exciton population $|1\rangle\langle 1|$. This could reduce the impact of DSFDs R_{18} and R_{22}.

Upon expansion, Eq. (1) features a factor of −1 between the third-order and fifth-order response functions. This produces a phase difference of $\phi = \pi$ between the third-order and the fifth-order coherences. There is an additional phase factor of $\phi = \pi$ every time a pulse interacts with the right (*bra*) side of the DSFD. In the spectral domain, this accumulated phase translates to a change in sign between respective response functions, R_i. This sign is given in brackets next to every response function R_i in Figs. 2–4.

The non-linear response probed in 2DES allows the separation of inhomogeneous and homogeneous linewidths. In QDs, the energy of the band-edge state is inversely proportional to the quantum dot diameter due to quantum confinement. Size heterogeneity in a sample of QDs thus causes inhomogeneous broadening in spectroscopic measurements.[42] In 2DES, inhomogeneous broadening is reflected as a broadening along the main diagonal due to correlation between the excitation energy E_1 and emission energy E_3.[36,43,44] This is shown schematically in Fig. 5(a). The excitation and emission energies both blueshift with the decreasing particle size. Inhomogeneous broadening has also been observed in 2Q–1Q correlation maps.[16,45,46] This is schematically depicted for a fifth-order 2Q spectrum in Fig. 5(b), reflecting how the transition energies that are probed in a 2Q experiment may reflect an inhomogeneous particle size distribution.

A phenomenological model is developed in Figs. 5(c) and 5(d) to qualitatively describe the effect of sample inhomogeneity on both 1Q and 2Q spectra. A simulated 2DE spectrum for a single, fully

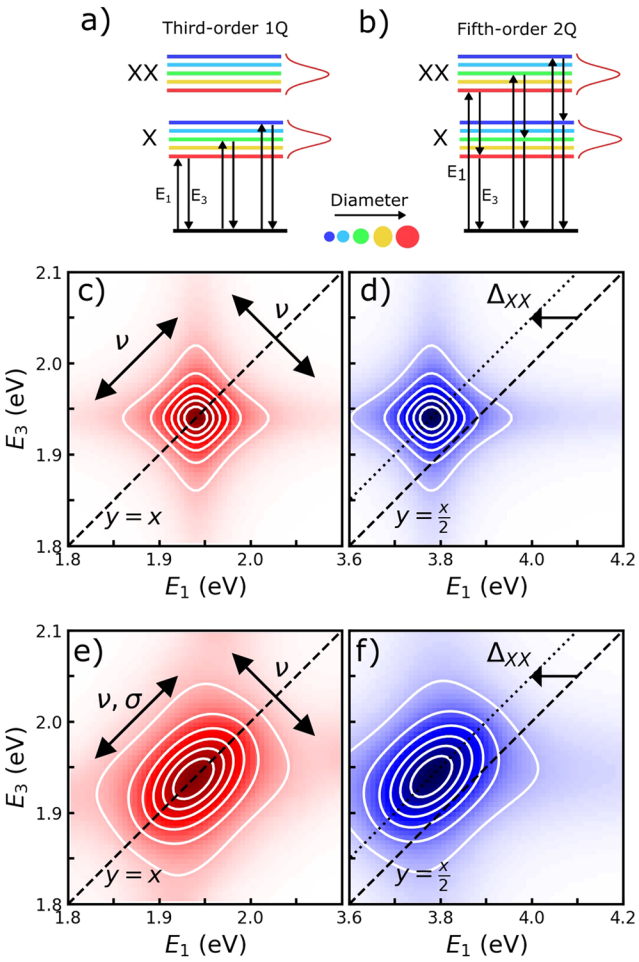

FIG. 5. (a) Inhomogeneous broadening as probed by the 1Q stimulated emission pathway R_2. (b) Inhomogeneous broadening as probed by the fifth-order 2Q stimulated emission pathway R_{16}. 2D spectra correlate the energy of the first transition (E_1) with the energy of the third transition (E_3). Both E_1 and E_3 vary with the QD size and are thus correlated. (c) Simulated 1Q peak and (d) simulated 2Q peak. The lineshape is determined by the homogeneous broadening parameter ν. Panels (e) and (f) incorporate the inhomogeneous broadening parameter σ. The simulated fifth-order 2Q peak is redshifted by Δ_{XX} from the y = x/2 diagonal. Red represents a negative signal and blue represents a positive signal in panels (c)–(f).

absorptive, homogeneously broadened peak is shown in Fig. 5(c). The peak is generated by summing the simulated coherences from the rephasing SE diagram R_2 and the non-rephasing SE diagram R_5 and Fourier transforming the sum of the coherences. The coherences dephase at a rate of $\nu = 0.045$ PHz, leading to homogeneous broadening. The resulting spectrum lies on the main diagonal, y = x. In the simulated fifth-order 2Q spectrum in Fig. 5(d), the spectrum lies on the line $y = x/2 - \Delta_{XX}$. For the fifth-order 2Q spectrum, values of $\nu = 0.090$ PHz and $\Delta_{XX} = 100$ meV are used. Note that a different aspect ratio is used in panels (c) and (d), as well as panels (e) and (f). This choice of aspect ratios emphasizes the similarities and differences between the 1Q and 2Q spectra.

To incorporate inhomogeneous broadening, the spectra are convolved along the diagonal with a Gaussian distribution with widths of $\sigma = 40$ meV for the 1Q spectrum and $\sigma = 80$ meV for the 2Q spectrum. These spectra are shown in Figs. 5(e) and 5(f). The peaks are broadened along their respective diagonal lines. This model assumes that the biexciton energy does not vary across the inhomogeneous ensemble. In reality, the binding energy increases at smaller nanocrystal diameters,[2,47–49] which may be reflected in the tilt of the 2Q peaks. However, based on the known size-dependence of CdSe QDs,[47] we estimate that the binding energy does not vary enough through the size distribution of the sample to make an appreciable difference on the tilt of the 2Q peaks in this study.

IV. RESULTS AND DISCUSSION

Experimental 1Q and 2Q spectra are plotted in Fig. 6 for pump pulse energies of $I_0 = 2.9$ nJ/pulse, 13.5 nJ/pulse, and 35 nJ/pulse at $t_2 = 100$ fs. The population time is more than 4× the pulse length, so non-resonant signals caused by temporal overlap between pump and probe pulses are not expected. At $I_0 = 2.9$ nJ/pulse, a broad negative peak is seen in the 1Q spectrum along the diagonal line $E_1 = E_3$ with a minimum near $E_1 = E_3 = 1.94$ eV. This can be attributed to negative third-order GSB and SE pathways R_1, R_2, R_4, and R_5 with positive contributions from ESA pathways R_3 and R_6 attenuating the signal. The 2Q signal is expected to appear at roughly $E_1 = 2 \times 1.94 = 3.68$ eV, though no signal is seen in that region. At low pump intensity, pathways featuring a single interaction per pulse are dominant, so mainly third-order signals are observed and contributions from fifth-order 1Q and fifth-order 2Q pathways are minimal.

At higher pump intensity, multiple interactions per pulse become probable and fifth-order signals begin to appear. The 2Q signal manifests as a broad positive peak near the $E_1 = 2 \times E_3$ diagonal line, as expected. The 2Q signal begins to appear with $I_0 = 13.5$ nJ/pulse though the spectrum is contaminated with artifacts due to noise; therefore, this spectrum is included for purely illustrative purposes, and the spectral lineshape will not be interpreted. At $I_0 = 35.0$ nJ/pulse, the peak amplitude of the 2Q signal is 66% of the peak amplitude of the 1Q signal at $I_0 = 2.9$ nJ, resulting in a spectrum that is smooth enough for comparison with the 1Q spectra.

The fifth-order contributions to the 1Q spectrum are more subtle. With increasing pump intensity, a negative shoulder appears in the 1Q spectrum around $(E_1, E_3) = (1.88, 1.88)$ eV, as expected for

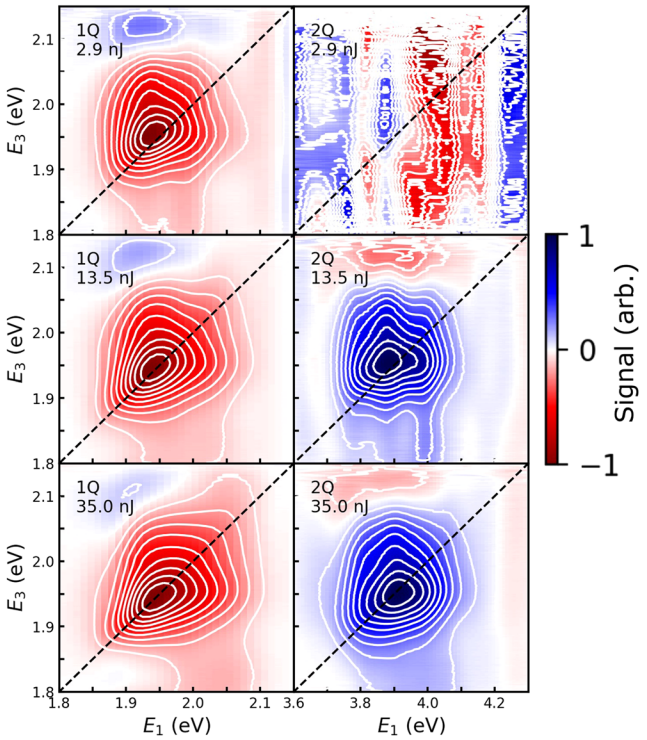

FIG. 6. 1Q and 2Q spectra at $t_2 = 100$ fs with pump pulse energies of $I_0 = 2.9$ nJ/pulse, 13.5 nJ/pulse, and 35 nJ/pulse, respectively. In the 1Q spectra, the dashed line corresponds to $E_1 = E_3$. In the 2Q spectra, the dashed line corresponds to $E_1 = 2E_3$. At $I_0 = 2.9$ nJ/pulse, only third-order contributions are present in the 1Q spectrum and no signal is seen in the range of the 2Q spectrum. As the pump intensity increases, fifth-order signals appear in both spectra. The sign of each spectrum reflects the sign of the DSFDs in Figs. 3 and 4.

fifth-order 1Q pathways R_8, R_9, R_{12}, and R_{13}. The 1Q peak narrows at $(E_1, E_3) = (1.88, 2.03)$ eV, consistent with a positive shoulder due to pathways R_7 and R_{11}. These features have been discussed in more detail in previous publications.[37,38]

Projections onto the emission axis, E_3, reflect emission energies. All the third-order 1Q, fifth-order 1Q, and fifth-order 2Q pathways have 1Q coherences on the emission axis. The 1Q and 2Q 2D spectra thus appear in a similar spectral region when projected onto E_3. However, inhomogeneous broadening and fifth-order contributions to the 1Q spectra must be taken into account when comparing the E_3 projections of the 1Q and 2Q 2D spectra.

E_3 projections are also known as pseudo-TA projections because they conceptually resemble transient absorption (TA) spectra. Under high pump intensity, ESA is diminished in band-edge TA spectra of CdSe QDs as the XX state becomes saturated.[37] The band-edge TA spectrum then resembles the linear absorption spectrum.[37,47] Figure 7(a) shows E_3 projections produced by integrating across the full excitation range, from $E_1 = 1.8$ eV–2.1 eV for the 1Q 2D spectrum or $E_1 = 3.6$ eV–4.2 eV for the 2Q 2D spectrum. The spectra are set to 0 at 1.8 eV and 1 at their maxima. The projections closely follow the linear absorption spectrum, consistent with

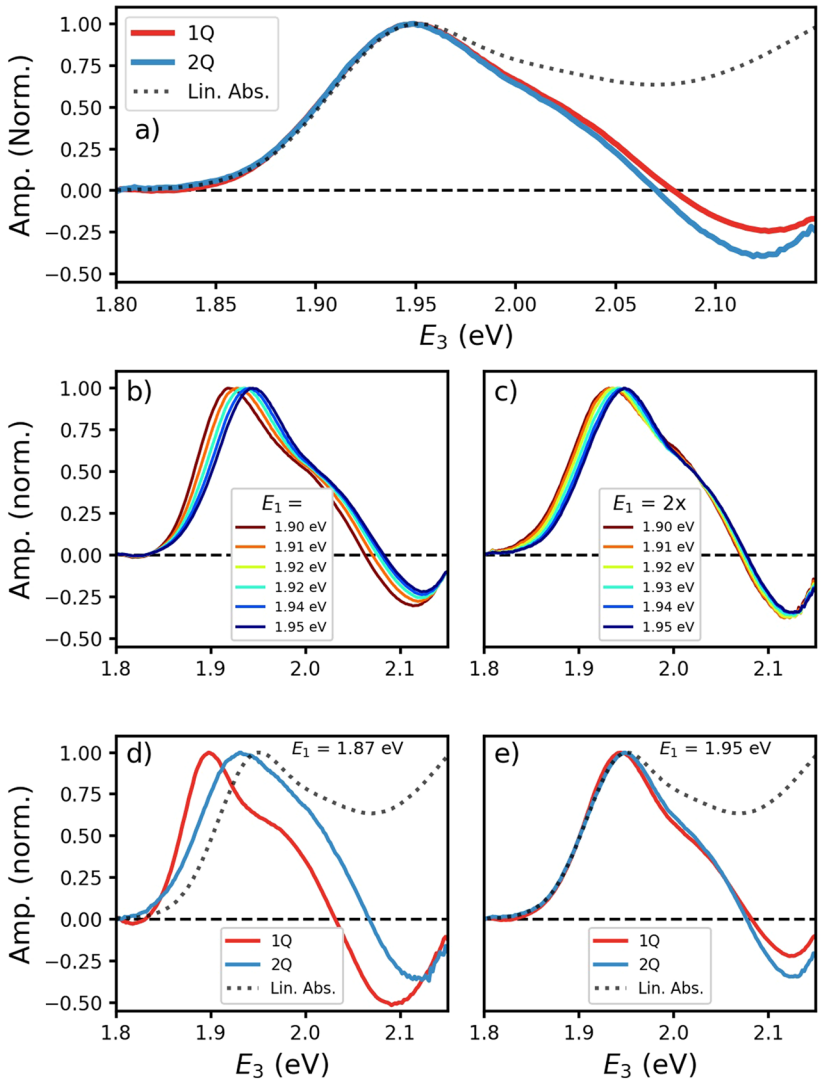

FIG. 7. Experimental E_3 projections at t_2 = 100 fs and with a pulse energy of 35 nJ/pulse. Spectra are normalized to their absolute maxima, which changes the sign of the 1Q spectrum. (a) Integrated E_3 projections show the similarity between the 1Q and 2Q spectra, consistent with the behavior of these systems at high fluence. Consecutive E_3 projections at a range of E_1 values reflect inhomogeneous broadening in (b) 1Q spectra and (c) 2Q spectra. Fifth-order 1Q contributions to the 1Q spectra cause deviations between the 1Q and 2Q signals. This discrepancy can be seen at E_1 = 1.87 (d), but not at E_1 = 1.95 (e).

the high pump intensity transient absorption studies on the same material.[37,47] Pseudo-TA spectra at a range of pump intensities show a peak that redshifts with increasing pump intensity for both 1Q 2D and 2Q 2D spectra, consistent with ESA pathways blocked by saturation of the XX state (Appendix A 4).

The normalized integrated projections in Fig. 7(a) are nearly identical for the 1Q and 2Q experiments though there is a clear deviation around E_3 = 2.10 eV. Spectral features in this region can be attributed to mixed multi-exciton states, incorporating exciton states other than the band-edge state, and cannot be rationalized by a three level system.[37] Both the 1Q and 2Q spectra feature ESA contributions from X to mixed XX states as well as ESA from XX to mixed XXX states.

One of the advantages of 2DES over TA is an increased resolution in excitation energies. Figure 7(b) shows a sequence of 1Q pseudo-TA spectra taken at a range of excitation energies. Increased excitation energy shifts the pseudo-TA spectra to higher energies. This reflects the inhomogeneous broadening, previously discussed in Fig. 5. A similar trend is seen in the 2Q spectra, shown in Fig. 7(c).

Clear differences between the 1Q and 2Q spectra appear at specific excitation energies. Pseudo-TA slices through the 1Q 2D spectrum at E_1 = 1.95 eV and the 2Q 2D spectrum at E_1 = 2 × 1.95 eV in Fig. 7(e) resemble the integrated spectra in Fig. 7(a). However, pseudo-TA slices through the 1Q 2D spectrum at E_1 = 1.87 eV and the 2Q 2D spectrum at E_1 = 2 × 1.87 eV in Fig. 7(d) look considerably different. This can be attributed to fifth-order 1Q contributions that appear at lower values of E_1 in the 1Q 2D spectrum.

Due to the spectral overlap between the ESA and XX SE pathways in the 2Q spectra (as seen in Fig. 4), it is difficult to separate

their effects. Both the 1Q and 2Q signals saturate at high pump intensity, confirming that biexcitons are being formed (Appendix A 4). Therefore, one would expect the 1Q pathways R_{10} and R_{14} and the 2Q pathways R_{18} and R_{22} to create a deviation from the linear absorption spectrum in the E_3 projections. This deviation is not apparent in either the 1Q or 2Q spectra.

Figure 8 shows projections onto the excitation axis, E_1. These excitation spectra are complementary to the pseudo-TA spectra in Fig. 7. As seen in Fig. 6, the 2Q excitation axis lies at roughly twice the energy of the 1Q excitation axis. For easy comparison, the excitation axis of the 2Q 2D spectrum is divided by a factor of 2 and normalized. Integrated excitation spectra, generated by integrating along E_3 from 1.8 eV to 2.1 eV, are plotted in Fig. 8(a). The 1Q excitation projection closely follows the linear absorption spectrum, as expected. However, the 2Q excitation projection contains a spectral feature that is redshifted relative to the linear spectrum.

The DSFDs in Fig. 4 predict that the 2Q signal from the band-edge biexciton state would be redshifted due to the biexciton binding energy, Δ_{XX}. A similar result was previously reported,[50] where transient absorption experiments and atomistic many-body pseudopotential calculations showed a biexciton absorption spectrum redshifted relative to the single exciton absorption spectrum. The magnitude of the shift in Fig. 8(a) is 20 meV, as determined at half of the peak intensity. This would correspond to a binding energy on the order of 40 meV, as the 2Q spectrum was divided by a factor of 2. Transient absorption studies of similar sized CdSe QDs determine a binding energy in the range of 5 meV–10 meV.[37,50] 1Q 2DES

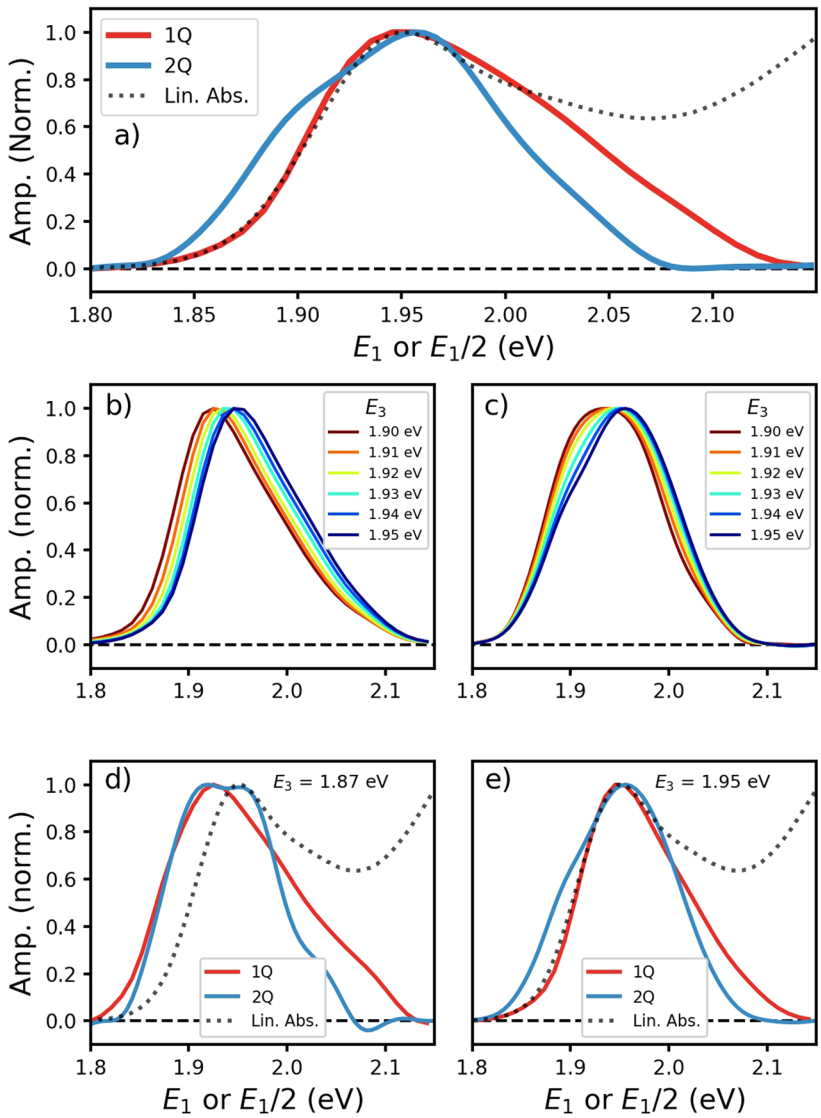

FIG. 8. Experimental E_1 projections at t_2 = 100 fs and I_0 = 35 nJ/pulse. Spectra are normalized to their absolute maxima, which changes the sign of the 1Q spectrum. (a) Integrated E_1 projections show that the 2Q spectrum is redshifted relative to the 1Q spectrum. E_1 projections at selected values of E_3 reflect inhomogeneous broadening in the (b) 1Q 2D spectrum and (c) 2Q 2D spectrum. E_1 projections at E_3 = 1.87 eV (d) do not show a shift between the 1Q and 2Q spectra, while E_1 projections at E_3 = 2.00 eV (e) do show a shift.

studies of CdSe QDs have already identified that there is a manifold of biexciton states, and some of these states have binding energies as high as $\Delta_{XX} = 65$ meV.[37,38] These biexciton states are only accessible at early population times and at specific excitation energies, so they require the high spectral and temporal resolution of 2DES. Figure 9 elaborates on how these biexcitonic states may be observed with 2Q 2DES.

The 2Q excitation spectrum in Fig. 8(a) also features a peak that is blueshifted relative to the 1Q excitation spectrum. This contradicts the model presented in Fig. 5 for an inhomogeneously broadened three level system, which predicted that the peak of the 2Q spectrum would be redshifted relative to the 1Q spectrum. We attribute this to biexciton states above the band-edge. Full modeling of the 2Q 2D spectrum therefore must incorporate the complete array of biexciton states that appear in the bandwidth. Additionally, the model must incorporate pulse spectrum effects that affect third-order and fifth-order spectra differently due to the different number of pulse interactions.[51,52]

Figure 8(b) shows a sequence of 1Q excitation spectra taken at a range of excitation energies. A corresponding set of spectra are shown in Fig. 8(c) for the 2Q experiment. These spectra reflect the same inhomogeneous broadening as the pseudo-TA projections in Figs. 7(b) and 7(c) but may also reflect different spectral features originating from GSB, SE, and ESA. Comparison of 1Q and 2Q excitation spectra at specific emission energies thus may result in different values for the biexciton binding energy.

The excitation spectra through the peak at $E_3 = 1.95$ eV in Fig. 8(e) show the same trend as the integrated spectra in Fig. 8(a). However, the excitation spectra at energies below the peak at $E_3 = 1.87$ eV in Fig. 8(d) do not show the redshift between the 1Q and 2Q signals. This reflects the fifth-order 1Q contributions to the 1Q spectrum as these would appear at lower values of E_1. Comparison of E_1 projections of 1Q and 2Q 2D spectra theoretically presents a wealth of information about X and XX states, though inhomogeneous broadening and fifth-order 1Q contributions to the 1Q spectra must be taken into account.

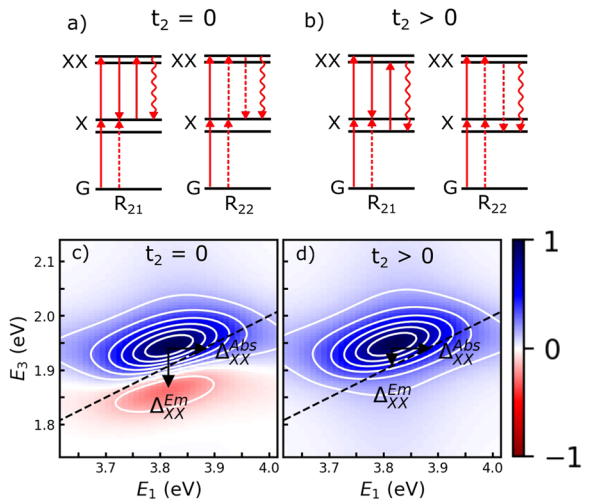

FIG. 9. The transitions in certain fifth-order pathways may change from $t_2 = 0$ to $t_2 > 0$ [panels (a) and (b), respectively] due to population relaxation between the second and third pulses. Therefore, projections onto the absorption (E_1) and emission (E_3) axes may reveal different biexciton binding energies. (c) Simulated fifth-order 2Q spectrum at $t_2 = 0$. (d) Simulated fifth-order 2Q spectrum at $t_2 > 0$.

Both the X and XX states feature a fine structure and therefore cannot be accurately described by a simple three level system.[2,37] Previous 1Q 2D studies have showed that different transitions between X and XX may be favored as the population time, t_2, progresses.[37,38] The low energy states in the 2Q projection in Fig. 8(a) appear to contradict transient absorption studies, but this may be understood by considering a population that relaxes through the X and XX fine structures during t_2.

Figure 9(a) shows two fifth-order 2Q pathways at $t_2 = 0$. In R_{21}, the first pulse raises the *ket* to an XX state, and the energy of this transition reflects a certain binding energy, Δ_{XX}^{Abs}. The second pulse creates an X population. The third pulse then excites the *ket* from X to XX and the energy of this transition also reflects a certain binding energy, Δ_{XX}^{Em}. As the time delay between the second and third pulse is 0 fs, one may assume that the system did not change states between the second and third pulse and that $\Delta_{XX}^{Em} = \Delta_{XX}^{Abs}$. Figure 9(b) shows the same pathway at $t_2 > 0$. Between the second and third pulses, an exciton may relax to another state within the fine structure of X. After t_2, the third pulse would then excite the *ket* from X to XX but the energy of this transition may reflect a different binding energy, $\Delta_{XX}^{Em} \neq \Delta_{XX}^{Abs}$. Therefore, excited state absorption processes and 2Q absorption processes could reveal different binding energies. A similar phenomenon would apply to R_{22}, though it is the XX population that evolves during t_2 and the transition induced by the third pulse is reversed.

Figures 9(c) and 9(d) show simulated fifth-order 2Q spectra at $t_2 = 0$ and $t_2 > 0$, respectively. The spectra show a single positive peak for pathways R_{15}, R_{16}, R_{19}, and R_{20} and a single negative peak for pathways R_{17}, R_{18}, R_{21} and R_{22}. Values of $\Delta_{XX}^{Abs} = \Delta_{XX}^{Em}(t_2 = 0) = 65$ meV and $\Delta_{XX}^{Em}(t_2 > 0) = 10$ meV were used. As t_2 progresses, the E_1 positions of both peaks do not change because E_1 reflects pulse interactions that occur before the population time delay. However, the lineshape along E_3 may vary as states that would lead to lower energy excitated state absorption transitions (i.e., larger binding energies) become depopulated. At late population times, the negative peak does not appear as a separate feature but rather an attenuation of the positive peak, as in the 2Q spectrum Fig. 6. A biexciton state with a binding energy of 65 meV has been identified using 1Q 2DES by monitoring the excited state absorption at early population times before population relaxation, as in Fig. 9(c), and measuring the position of the excited state absorption peak along E_3.[37,38] This same state may be reflected in 2Q 2DES in the form of the Δ_{XX}^{Abs} peak shift, which would not vary with population time. This is an advantage of 2Q 2DES over 1Q 2DES as the spectra are less crowded and the spectra contain information about the 2Q coherences even at late population times.

The E_1 projection seen in Fig. 8(a) therefore may be explained by a combination of factors: 2D spectra have higher spectral resolution than transient absorption spectra; the 2Q 2D spectra presented here isolate fifth-order signals, while 1Q 2D spectra are crowded with both third-order and fifth-order contributions; population relaxation through a ladder of fine structure states favors

different transitions in excited state absorption and 2Q absorption; fifth-order lineshapes are inherently different from third-order lineshapes due to pulse shape effects.[51,52] Further studies are required to deconvolve these effects.

The presence of the X and XX manifolds also complicates interpretation of the fifth-order 2Q spectra as some of the transitions between X and XX may be near-degenerate, resulting in ambiguity in peak assignment. This is particularly the case for the R_{21} and R_{22} pathways as these signals have the same sign and peak position, while the former reflects dynamics in X and the latter dynamics in XX. Careful population time studies may be able to isolate these dynamics. Varying the pump pulse intensity could also help in this discrimination as the intensity of R_{21} should diminish with increasing pump intensity and vice-versa for R_{22}.

V. CONCLUSION

Fully absorptive third-order and fifth-order spectroscopy was simultaneously conducted on colloidal CdSe quantum dots using phase-cycling in the pump–probe geometry. Fifth-order 2Q spectroscopy was conducted at population times several times longer than the pulse duration, avoiding non-resonant artifacts due to the temporal overlap of pump and probe pulses. Fifth-order 2Q signals only appeared at high fluences, indicating that the 2Q signal only appears with substantial intensity when multi-excitons are formed in the QDs. The fully absorptive lineshape of the 2Q 2D spectrum allowed for easy comparison with the 1Q 2D spectrum. Comparison of 1Q and 2Q 2D spectra aligned with theoretical predictions only when inhomogeneous broadening and fifth-order 1Q contributions to the 1Q spectra were taken into account. A biexciton excitation spectrum was measured by projecting the 2Q 2D spectrum onto its excitation axis, and this spectrum extends to energies lower than those predicted by excited state absorption signals. Further studies, at a larger range of population times and a variety of QD sizes, may reveal more details of dynamics within the biexciton fine structure.

ACKNOWLEDGMENTS

We acknowledge CFI, NSERC, FQRNT, and McGill University for funding. Hélène Seiler further acknowledges the Swiss National Science Foundation for their scholarship and support under Grant No. P2SKP2 184100. We would like to thank Daniel Turner for his helpful comments.

APPENDIX A: ADDITIONAL EXPERIMENTAL DETAILS

1. Linear absorption spectrum

The energy of the X_1 state, 1.94 eV, is determined by fitting the absorption spectrum as measured in a Cary UV/vis spectrometer in a 1 cm cuvette (Fig. 10). The spectrum of the laser used in the 2DE experiment covers the first two excited states, X_1 = 1.94 eV and X_2 = 2.01 eV, and finite pulse effects are not expected in the region of the X_1 peak.

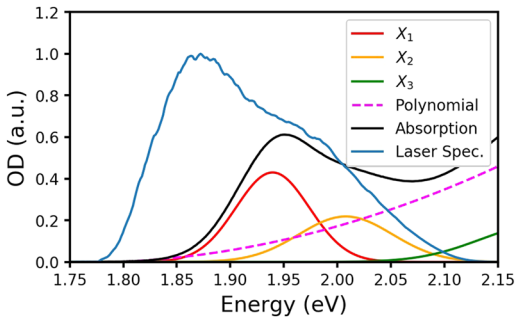

FIG. 10. Absorption spectrum and constituent peaks, X_1, X_2, and X_3. Laser spectrum determined at the sample position.

2. Pulse characterization

The pulse from the pump beam pulse shaper was characterized with transient grating frequency resolved optical gating (TG-FROG), shown in Fig. 11. The pulse was created using the same conditions as the I_0 = 35 nJ/pulse experiment presented above, though a single pulse was created by the pulse shaper resulting in a pulse energy of I_0 = 70 nJ/pulse. The time marginal of the TG-FROG trace has a Gaussian shape with a FWHM of 17 fs, corresponding to a pulse duration of 12 fs. Saturation effects in the pulse shapers may lead to changes in the pulse shape as the intensity of the pulse is increased. The TG-FROG confirms that the pulse is compressed and symmetrical at high intensity. Therefore, it is assumed that pulse shaper saturation effects do not significantly alter the pulse shape within the range of pulse intensities used in this study.

3. Apodization

Figure 12 shows the coherences measured in the 1Q and 2Q experiments. Apodization windows are chosen with a short enough

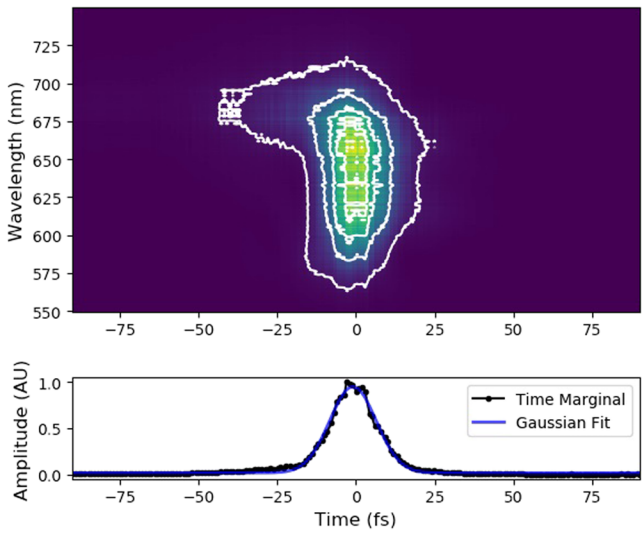

FIG. 11. Frequency resolved optical gating (FROG) trace and corresponding time marginal.

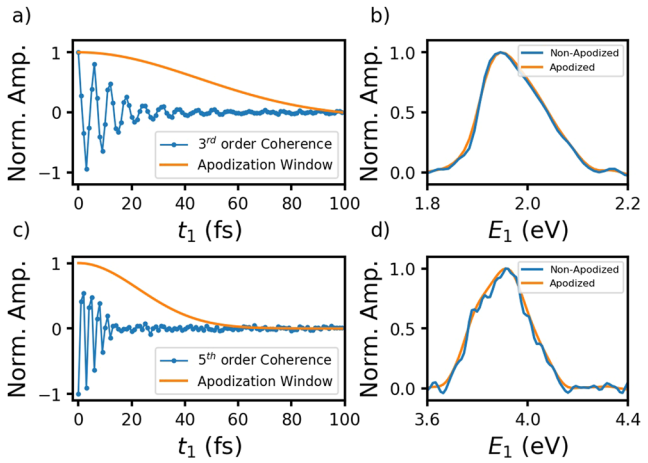

FIG. 12. (a) Coherence during t_1 for the 1Q experiment, integrated across emission energies. Apodization window consisting of a Gaussian distribution centered at $t_1 = 0$ with $\sigma = 45$ fs. (b) Fourier transform of coherence in (a), apodized and non-apodized. (c) Coherence during t_1 for the 2Q experiment, integrated across emission energies. Apodization window consisting of a Gaussian distribution centered at $t_1 = 0$ with $\sigma = 22.5$ fs. (d) Fourier transform of coherence in (c), apodized and non-apodized.

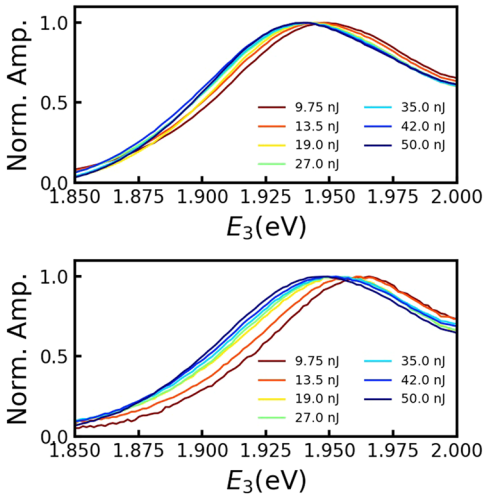

FIG. 14. Top: 1Q 2D pseudo-TA spectra at $E_1 = 1.95$ eV and $t_2 = 100$ fs. Bottom: 2Q 2D pseudo-TA spectra at $E_1 = 1.95$ eV and $t_2 = 100$ fs.

width that they will minimize the effect of noise at late coherence times and a long enough width so that they do not significantly alter the dephasing of the coherences. This is reflected in the spectral domain as noise is removed from the spectra, but the overall lineshape is not significantly changed.

4. Pump intensity

Figure 13(a) shows the signal amplitude of the 1Q and 2Q 2D spectra as a function of the pump energy per pulse, I_0, at $t_2 = 100$ fs. The amplitude is taken at $E_1 = E_3 = 1.94$ eV for the 1Q spectrum and $E_1/2 = E_3 = 1.94$ eV for the 2Q spectrum.

The 1Q signal saturates at high pump intensities as the number of single excitons and biexcitons reaches equilibrium.[37] This is attributed to the band-edge electronic state having a degeneracy of 2. The 1Q signal saturates at around $I_0 = 20$ nJ/pulse. This confirms that a significant population of biexcitons is present in the sample at the pump energies used in the experiments in this paper,

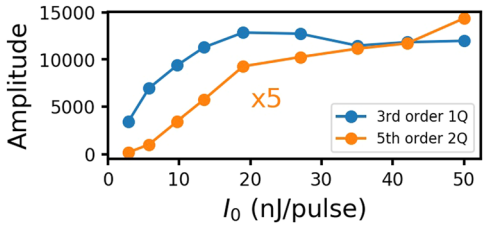

FIG. 13. Signal for the 1Q and 2Q signals at $t_2 = 100$ fs at $E_1 = E_3 = 1.94$ eV for the 1Q spectrum and $E_1/2 = E_3 = 1.94$ eV for the 2Q spectrum.

$I_0 = 35$ nJ/pulse. The 2Q 2D signal begins to show signs of saturation at the same pump intensity. This is consistent with the 2Q 2D signal in that region primarily originating from the band-edge electronic state.

Pseudo-TA spectra at $E_1 = 1.95$ eV and $E_1/2 = 1.95$ eV for 1Q and 2Q spectra, respectively, are shown in Fig. 14. The peak redshifts with increasing pump intensity in both cases.

APPENDIX B: PHASE CYCLING SCHEME

In the pump–probe geometry, the two collinear excitation pulses are followed by a non-collinear probe pulse. The desired signals are therefore retrieved by a combination of wavevector selection and phase-cycling. Appendix B 1 reviews how the signal wavevectors are used to narrow down the number of detected signals. Appendix B 2 reviews how phase-cycling is used to retrieve specific signals.

1. Wavevector selection

A signal field of order K is given by the following equation:

$$E^{(K)}(\vec{\alpha}_j, \vec{\phi}, t_1, t_2, t_3) \propto e^{i(\alpha_{1j}\phi_1 + \alpha_{2j}\phi_2 + \alpha_{3j}\phi_3)} R^{(K)}_{\vec{\alpha}_j}(t_1, t_2, t_3). \quad \text{(B1)}$$

The phase of each pulse is given by the vector $\vec{\phi} = (\phi_1, \phi_2, \phi_3)$. These phases are user-defined and imparted on the signal field by the pulse shapers. Each signal field is labeled with a coherence transfer vector $\vec{\alpha}_j = (\alpha_{1j}, \alpha_{2j}, \alpha_{3j})$, with $\alpha_{ij} \in \mathbb{Z}$. Each coherence transfer step α_{ij}'s represents the number of times excitation field E_i acts on the right side of the DSFD minus the number of times it acts on the left side for a given pathway j. The emitted signal field is given by the sum of the fields corresponding to each coherence transfer vector $\vec{\alpha}_j$,

$$E^{(K)}(\vec{\phi}, t_1, t_2, t_3) = \sum_{j=1}^{N_{\vec{\alpha}}} E^{(K)}(\vec{\alpha}_j, \vec{\phi}, t_1, t_2, t_3)$$
$$= \sum_{j=1}^{N_{\vec{\alpha}}} e^{i\vec{\alpha}_j \cdot \vec{\phi}} \mathrm{R}_{\vec{\alpha}_j}^{(K)}(t_1, t_2, t_3), \quad \text{(B2)}$$

where $N_{\vec{\alpha}}$ is the number of coherence transfer vectors. The number of terms in this sum can be limited by taking into account three conditions. Equation (B3) ensures we are not considering contributions due to multiple harmonic generation. Equation (B4) is the phase-matching condition in the pump–probe geometry, with $k_1 = k_2$. Equation (B5) states that signals above order K will be neglected,

$$\sum_{i=1}^{n} \alpha_{ij} = 1, \quad \text{(B3)}$$

$$\sum_{i=1}^{n-1} \alpha_{ij} = 0, \quad \text{(B4)}$$

$$\sum_{i=1}^{n} |\alpha_{ij}| \leq K \in \mathbb{N}. \quad \text{(B5)}$$

In the preceding equations, i is the pulse index and n is the number of pulses. The signal fields acquired by expanding Eq. (B2) and applying the conditions in Eqs. (B3)–(B5) are given in Table I for a fifth-order, three pulse experiment ($K = 5$, n = 3). Note: the labels for the response functions R_i in this appendix do not correspond to the response functions in the main text.

The third field, R_3, describes linear, pump–probe as well as reverse transient-grating signals from the probe pulse. This contribution is generally undesired and will be removed by phase-cycling. The fully absorptive 1Q and 2Q signals can be retrieved by isolating $R^{(3)} = R_2 + R_4$ and $R^{(5)} = R_1 + R_5$, respectively. These signals will be separated by phase-cycling.

2. Phase-cycling

When phase-cycling, a phase ϕ_{li} is imparted on pulse i at the phase-cycling step l. In a 4 × 1 × 1 phase-cycling scheme, the first pulse is cycled through a sequence of four phases, $\phi = (0, \pi/2, \pi, \text{and } 3\pi/2)$. The signal $S_{\text{abs,j}}$ is given by a weighted sum of the intensity $I_l(\phi)$ at every step in the cycle,

TABLE I. Possible fields of order 5 or less for a three pulse experiment in the pump–probe geometry. Obtained from solving Eqs. (B2)–(B5) for $n = 3$ and $K = 5$.

Signal field	Label	α_{1j}	α_{2j}	α_{3j}	ψ_j
$E_{\vec{\alpha}_1}$	R_1	−2	2	1	$-2\phi_1 + 2\phi_2 + \phi_3$
$E_{\vec{\alpha}_2}$	R_2	−1	1	1	$-\phi_1 + \phi_2 + \phi_3$
$E_{\vec{\alpha}_3}$	R_3	0	0	1	ϕ_3
$E_{\vec{\alpha}_4}$	R_4	1	−1	1	$\phi_1 - \phi_2 + \phi_3$
$E_{\vec{\alpha}_5}$	R_5	2	−2	1	$2\phi_1 - 2\phi_2 + \phi_3$

$$S_{\text{abs,j}}(t_1, t_2, \omega_3) = W_{j1} I_1(\phi_{11} = 0) + W_{j2} I_2(\phi_{21} = \pi/2) + W_{j3} I_3(\phi_{31} = \pi) + W_{j4} I_4(\phi_{41} = 3\pi/2). \quad \text{(B6)}$$

To retrieve the signal $S_{\text{abs,j}}$ for a specific coherence transfer vector j, we must find the appropriate weights by calculating the weight factors matrix $\boldsymbol{W}$.

Before defining $\boldsymbol{W}$, we must first build the phase matrix $\boldsymbol{\Psi}$, given by Eq. (B7). The coherence transfer step matrix $\boldsymbol{\alpha}$, where α_{ij} is the net coherence transfer step, is imparted by pulse i in pathway R_j. The size of $\boldsymbol{\alpha}$ is $(n \times N_{\vec{\alpha}})$. The phases of the pulses are user-defined and are given by matrix $\boldsymbol{\phi}$, where $\boldsymbol{\phi_{li}}$ is the phase of pulse i at the phase-cycling step l. The size of $\boldsymbol{\phi}$ is $(N \times n)$, where N is the number of phase-cycling steps,

$$\boldsymbol{\Psi} = \boldsymbol{\phi}\boldsymbol{\alpha}. \quad \text{(B7)}$$

The coefficient $\boldsymbol{\Psi_{lj}}$ is the phase of the signal arising from R_j during the phase-cycling step l. For example, for the 4 × 1 × 1 phase-cycling scheme introduced for the fifth-order, the three pulse experiment $\boldsymbol{\Psi}$ is expressed as

$$\boldsymbol{\Psi} = \begin{pmatrix} 0 & 0 & 0 & 0 & 0 \\ \pi & \frac{3\pi}{2} & 0 & \frac{\pi}{2} & \pi \\ 0 & \pi & 0 & \pi & 0 \\ \pi & \frac{\pi}{2} & 0 & \frac{3\pi}{2} & \pi \end{pmatrix}.$$

From $\boldsymbol{\Psi}$, it is possible to build the weight factors matrix $\boldsymbol{W}$,

$$W_{jl} = e^{-i\Psi_{lj}}, \quad \text{(B8)}$$

where $\boldsymbol{W}$ is of size $(N_{\vec{\alpha}} \times N)$. The weight matrix prescribes the prefactors to use when summing the measured intensity, as in Eq. (B6). For the 4 × 1 × 1 phase-cycling scheme, it is given by

$$\boldsymbol{W} = \begin{pmatrix} 1 & -1 & 1 & -1 \\ 1 & i & -1 & -i \\ 1 & 1 & 1 & 1 \\ 1 & -i & -1 & i \\ 1 & -1 & 1 & -1 \end{pmatrix},$$

where labels W_j denote the row vectors. From $\boldsymbol{\Psi}$, it is also possible to build a signal field matrix element-wise,

$$E_{lj} = \mathrm{R}_j \cdot e^{i\Psi_{lj}}, \quad \text{(B9)}$$

where $\boldsymbol{E}$ is of size $(N \times N_{\vec{\alpha}})$. In this matrix, column j represents the phases taken by the field associated with pathway R_j throughout the phase-cycling procedure. The sum of the coefficients over a given row represents the total signal field emitted from the sample for a given phase-cycling step, as per Eq. (B1),

$$\boldsymbol{E} = \begin{pmatrix} -\mathrm{R}_1 & -\mathrm{R}_2 & -\mathrm{R}_3 & -\mathrm{R}_4 & -\mathrm{R}_5 \\ \mathrm{R}_1 & -i\mathrm{R}_2 & -\mathrm{R}_3 & i\mathrm{R}_4 & \mathrm{R}_5 \\ -\mathrm{R}_1 & \mathrm{R}_2 & -\mathrm{R}_3 & \mathrm{R}_4 & -\mathrm{R}_5 \\ \mathrm{R}_1 & i\mathrm{R}_2 & -\mathrm{R}_3 & -i\mathrm{R}_4 & \mathrm{R}_5 \end{pmatrix}.$$

Then, the phase-cycling scheme can be quickly assessed using matrix multiplication,

$$\tilde{\boldsymbol{E}} = \boldsymbol{W} \cdot \boldsymbol{E}. \tag{B10}$$

It is easy to verify that for the 4 × 1 × 1 scheme,

$$\tilde{\boldsymbol{E}} = \begin{pmatrix} 4R_1 & 0 & 0 & 0 & 4R_5 \\ 0 & 4R_2 & 0 & 0 & 0 \\ 0 & 0 & 4R_3 & 0 & 0 \\ 0 & 0 & 0 & 4R_4 & 0 \\ 4R_1 & 0 & 0 & 0 & 4R_5 \end{pmatrix}.$$

This demonstrates that using weights $W_1 = W_5 = (1, -1, 1, -1)$ will simultaneously give R_1 and R_5, as desired for $R^{(5)}$. The third-order rephasing and non-rephasing signals are given separately by weights $W_2 = (1, i, -1, -i)$ and $W_4 = (1, -i, -1, i)$, respectively.

3. Optical detection

In the fully non-collinear geometry, a weak local oscillator E_{LO} is emitted in the phase-matching direction of the signal E_{sig} and both fields mix onto the detector array. In the pump–probe geometry, the third excitation field or probe field acts as the local oscillator. Neglecting scatter from other pulses, the CCD receives in this case

$$\begin{aligned} I(\omega) &= |E_{sig}(\omega) + E_{LO}(\omega)|^2 \\ &= \left| \sum_{j=1}^{5} E_{\alpha_j} + E_3(\omega) \right|^2, \end{aligned} \tag{B11}$$

where ω is the frequency at the detector. Expanding Eq. (B11) results in 21 terms. We can neglect any term not interfering with the probe field, E_3, as it will have a very low intensity. Five terms remain, corresponding to the five terms $E_{\vec{\alpha}_j}$ in Eq. (B11), each individually interfering with the probe field E_3,

$$I(\omega) = \sum_{j=1}^{5} I_j(\omega), \tag{B12}$$

where $I_j(\omega) = |E_{\alpha_j} E_3|$. We can write out an equivalent of Eq. (B10) in terms of intensity,

$$\vec{S} = \mathbf{W} \cdot \vec{I}. \tag{B13}$$

The $\vec{S}$ vector contains the results of the weighted sum as given in Eq. (B6) and is, in general, a complex signal,

$$\begin{pmatrix} S_1 \\ S_2 \\ S_3 \\ S_4 \\ S_5 \end{pmatrix} = \begin{pmatrix} 1 & -1 & 1 & -1 \\ 1 & i & -1 & -i \\ 1 & 1 & 1 & 1 \\ 1 & -i & -1 & i \\ 1 & -1 & 1 & -1 \end{pmatrix} \cdot \begin{pmatrix} I(\omega, 0) \\ I(\omega, \pi/2) \\ I(\omega, \pi) \\ I(\omega, 3\pi/2) \end{pmatrix}.$$

Following Eq. (B13), one can explicitly compute the signals for the coherence transfer vectors given in Table I. For example, $R^{(5)}$ is given by

$$S_1 = I(\omega, 0) - I(\omega, \pi/2) + I(\omega, \pi) - I(\omega, 3\pi/2). \tag{B14}$$

DATA AVAILABILITY

The data that support the findings of this study are available from the corresponding author upon reasonable request.

REFERENCES

[1] J. Shumway, A. Franceschetti, and A. Zunger, Phys. Rev. B **63**, 155316 (2001).
[2] M. Korkusinski, O. Voznyy, and P. Hawrylak, Phys. Rev. B **82**, 245304 (2010).
[3] A. V. Rodina and A. L. Efros, Phys. Rev. B **82**, 125324 (2010).
[4] P. Kambhampati, J. Phys. Chem. Lett. **3**, 1182 (2012).
[5] F. Šanda, V. Perlík, C. N. Lincoln, and J. Hauer, J. Phys. Chem. A **119**, 10893 (2015).
[6] A. F. Fidler, E. Harel, and G. S. Engel, J. Phys. Chem. Lett. **1**, 2876 (2010).
[7] N. H. Lewis, H. Dong, T. A. Oliver, and G. R. Fleming, J. Chem. Phys. **142**, 174202 (2015).
[8] S. Mukamel, R. Oszwałdowski, and L. Yang, J. Chem. Phys. **127**, 221105 (2007).
[9] J. Kim, V. M. Huxter, C. Curutchet, and G. D. Scholes, J. Phys. Chem. A **113**, 12122 (2009).
[10] K. W. Stone, K. Gundogdu, D. B. Turner, X. Li, S. T. Cundiff, and K. a. Nelson, Science **324**, 1169 (2009).
[11] D. B. Turner and K. A. Nelson, Nature **466**, 1089 (2010).
[12] D. Karaiskaj, A. D. Bristow, L. Yang, X. Dai, R. P. Mirin, S. Mukamel, and S. T. Cundiff, Phys. Rev. Lett. **104**, 117401 (2010).
[13] J. Dostál, F. Fennel, F. Koch, S. Herbst, F. Würthner, and T. Brixner, Nat. Commun. **9**, 2466 (2018).
[14] T. A. Gellen, L. A. Bizimana, W. P. Carbery, I. Breen, and D. B. Turner, J. Chem. Phys. **145**, 064201 (2016).
[15] F. Ding, E. C. Fulmer, and M. T. Zanni, J. Chem. Phys. **123**, 094502 (2005).
[16] E. C. Fulmer, F. Ding, and M. T. Zanni, J. Chem. Phys. **122**, 034302 (2005).
[17] G. Moody, R. Singh, H. Li, I. A. Akimov, M. Bayer, D. Reuter, A. D. Wieck, and S. T. Cundiff, Phys. Rev. B **87**, 041304 (2013).
[18] Z. Zhang, K. L. Wells, M. T. Seidel, and H.-S. Tan, J. Phys. Chem. B **117**, 15369 (2013).
[19] Z. Zhang, P. H. Lambrev, K. L. Wells, G. Garab, and H. S. Tan, Nat. Commun. **6**, 7914 (2015).
[20] D. B. Turner, P. Wen, D. H. Arias, and K. A. Nelson, Phys. Rev. B **84**, 165321 (2011).
[21] J. Süß, J. Wehner, J. Dostál, T. Brixner, and V. Engel, J. Chem. Phys. **150**, 104304 (2019).
[22] J. Süß and V. Engel, J. Chem. Phys. **152**, 174305 (2020).
[23] P. Malý, J. Lüttig, A. Turkin, J. Dostál, C. Lambert, and T. Brixner, Chem. Sci. **11**, 456 (2020).
[24] C. Heshmatpour, J. Hauer, and F. Šanda, Chem. Phys. **528**, 110433 (2020).
[25] B. Brüggemann and T. Pullerits, New J. Phys. **13**, 025024 (2011).
[26] A. Nemeth, F. Milota, T. Mančal, T. Pullerits, J. Sperling, J. Hauer, H. F. Kauffmann, and N. Christensson, J. Chem. Phys. **133**, 094505 (2010).
[27] T. Zhang, C. N. Borca, X. Li, and S. T. Cundiff, Opt. Express **13**, 7432 (2005).
[28] F. D. Fuller and J. P. Ogilvie, Annu. Rev. Phys. Chem. **66**, 667 (2015).
[29] D. Keusters, H.-S. Tan, and W. S. Warren, J. Phys. Chem. A **103**, 10369 (1999).
[30] W. Wagner, C. Li, J. Semmlow, and W. S. Warren, Opt. Express **13**, 3697 (2005).
[31] H.-S. Tan, J. Chem. Phys. **129**, 124501 (2008).
[32] S. Mueller, S. Draeger, X. Ma, M. Hensen, T. Kenneweg, W. Pfeiffer, and T. Brixner, J. Phys. Chem. Lett. **9**, 1964 (2018).
[33] S. Mueller, J. Lüttig, P. Malý, L. Ji, J. Han, M. Moos, T. B. Marder, U. H. Bunz, A. Dreuw, C. Lambert, and T. Brixner, Nat. Commun. **10**, 4735 (2019).
[34] J. R. Caram, H. Zheng, P. D. Dahlberg, B. S. Rolczynski, G. B. Griffin, D. S. Dolzhnikov, D. V. Talapin, and G. S. Engel, J. Chem. Phys. **140**, 084701 (2014).

[35]T. A. Gellen, J. Lem, and D. B. Turner, Nano Lett. **17**, 2809 (2017).
[36]H. Seiler, S. Palato, and P. Kambhampati, J. Chem. Phys. **149**, 074702 (2018).
[37]S. Palato, H. Seiler, H. Baker, C. Sonnichsen, P. Brosseau, and P. Kambhampati, J. Chem. Phys. **152**, 104710 (2020).
[38]H. Seiler, S. Palato, C. Sonnichsen, H. Baker, and P. Kambhampati, Nano Lett. **18**, 2999 (2018).
[39]B. Brüggemann, P. Kjellberg, and T. Pullerits, Chem. Phys. Lett. **444**, 192 (2007).
[40]P. Hamm and M. Zanni, *Concepts and Methods of 2D Infrared Spectroscopy* (Cambridge University Press, 2011), pp. 1–286.
[41]D. A. Blank, L. J. Kaufman, and G. R. Fleming, J. Chem. Phys. **111**, 3105 (1999).
[42]S. A. Empedocles, D. J. Norris, and M. G. Bawendi, Phys. Rev. Lett. **77**, 3873 (1996).
[43]M. E. Siemens, G. Moody, H. Li, A. D. Bristow, and S. T. Cundiff, Opt. Express **18**, 17699 (2010).
[44]S. D. Park, D. Baranov, J. Ryu, B. Cho, A. Halder, S. Seifert, S. Vajda, and D. M. Jonas, Nano Lett. **17**, 762 (2017).
[45]J. Kim, S. Mukamel, and G. D. Scholes, Acc. Chem. Res. **42**, 1375 (2009).
[46]J. Tollerud and J. A. Davis, J. Opt. Soc. Am. B **33**, C108 (2016); arXiv:1602.01150.
[47]S. L. Sewall, R. R. Cooney, K. E. H. Anderson, E. A. Dias, D. M. Sagar, and P. Kambhampati, J. Chem. Phys. **129**, 084701 (2008).
[48]J. M. Caruge, Y. Chan, V. Sundar, H. J. Eisler, and M. G. Bawendi, Phys. Rev. B **70**, 085316 (2004).
[49]J. M. Elward and A. Chakraborty, J. Chem. Theory Comput. **9**, 4351 (2013); arXiv:1306.2110.
[50]S. L. Sewall, A. Franceschetti, R. R. Cooney, A. Zunger, and P. Kambhampati, Phys. Rev. B **80**, 081310 (2009).
[51]T. N. Do, M. F. Gelin, and H.-S. Tan, J. Chem. Phys. **147**, 144103 (2017).
[52]T. N. Do, L. Chen, A. K. Belyaev, H.-S. Tan, and M. F. Gelin, Chem. Phys. **515**, 119 (2018).